

Simulations of multi-contrast x-ray imaging using near-field speckles

Cite as: AIP Conference Proceedings **1696**, 020016 (2016); <https://doi.org/10.1063/1.4937510>
Published Online: 28 January 2016

Marie-Christine Zdora, Pierre Thibault, Julia Herzen, Franz Pfeiffer, and Irene Zanette



View Online



Export Citation

ARTICLES YOU MAY BE INTERESTED IN

[Simulations of x-ray speckle-based dark-field and phase-contrast imaging with a polychromatic beam](#)

Journal of Applied Physics **118**, 113105 (2015); <https://doi.org/10.1063/1.4931145>

[X-ray phase imaging with a paper analyzer](#)

Applied Physics Letters **100**, 124102 (2012); <https://doi.org/10.1063/1.3694918>

[Quantitative X-ray dark-field and phase tomography using single directional speckle scanning technique](#)

Applied Physics Letters **108**, 124102 (2016); <https://doi.org/10.1063/1.4944462>

Lock-in Amplifiers
up to 600 MHz



Simulations of multi-contrast x-ray imaging using near-field speckles

Marie-Christine Zdora^{*,†}, Pierre Thibault^{**}, Julia Herzen^{*}, Franz Pfeiffer^{*} and Irene Zanette^{‡,*}

^{*}*Lehrstuhl für Biomedizinische Physik, Physik-Department & Institut für Medizintechnik, Technische Universität München, 85748 Garching, Germany*

[†]*Diamond Light Source, Harwell Science and Innovation Campus, Didcot, Oxfordshire, OX11 0DE, United Kingdom and Department of Physics & Astronomy, University College London, London, WC1E 6BT, United Kingdom*

^{**}*Department of Physics & Astronomy, University College London, London, WC1E 6BT, United Kingdom*

[‡]*Diamond Light Source, Harwell Science and Innovation Campus, Didcot, Oxfordshire, OX11 0DE, United Kingdom*

Abstract. X-ray dark-field and phase-contrast imaging using near-field speckles is a novel technique that overcomes limitations inherent in conventional absorption x-ray imaging, i.e. poor contrast for features with similar density. Speckle-based imaging yields a wealth of information with a simple setup tolerant to polychromatic and divergent beams, and simple data acquisition and analysis procedures. Here, we present a simulation software used to model the image formation with the speckle-based technique, and we compare simulated results on a phantom sample with experimental synchrotron data. Thorough simulation of a speckle-based imaging experiment will help for better understanding and optimising the technique itself.

Keywords: x-ray microscopy, phase-contrast imaging, dark-field imaging, near-field speckles, wavefront simulations, synchrotron radiation
PACS: 41.50.+h, 42.30.Ms, 05.45.Pq, 07.05.Pj, 42.30.Rx

INTRODUCTION

Phase-contrast and dark-field x-ray imaging are developing, at synchrotron as well as at laboratory sources, as powerful tools for high-sensitivity two- and three-dimensional investigation of samples at the micrometer scale. They excel in visualising very small density differences, such as similar types of soft tissues, and in detecting unresolvable features causing a relevant small angle x-ray scattering signal, such as fibres or cracks [1]. For these reasons they have important applications especially in the biomedical field and in materials science. Recent results include Refs. [2, 3].

Among the several techniques developed in the last years, a method based on tracking of near-field speckles has several advantages [4–8]. The setup, data acquisition and analysis procedures are relatively simple, it provides multi-contrast signals in different directions, and it works well not only at synchrotron facilities, but also at polychromatic laboratory sources [9, 10]. Speckle-based imaging relies on the sample-induced distortions of a near-field speckle pattern produced by a static random phase modulator (e.g. a piece of sandpaper or a biological filter membrane) [11]. The working principles of the method and the procedures to retrieve the image signals are described in detail in Refs. [4, 5, 9].

Previous works on this technique are mainly focussed on experimental measurements and observations. However, simulation studies are very beneficial to thoroughly investigate the image formation process, the influence of different setup parameters on the reconstructed dark-field and phase-contrast signals, and different reconstruction algorithms [12]. Here, we describe a simulation framework to model near-field speckle-tracking imaging, and we validate the simulated results with measurements performed at a synchrotron using a phantom sample. This work is the first step towards the detailed investigation of the speckle-tracking technique under different conditions, and will aid in the understanding and optimisation of the method.

MATERIALS AND METHODS

Simulation framework

The numerical simulations of x-ray speckle tracking were carried out using an object-oriented framework written in Python with extensions in C++ [3, 13]. The framework has been successfully employed for quantitative grating-based phase-contrast and dark-field imaging [3, 14], and more recently for studies on the effects of the polychromaticity of the x-ray beam on the images retrieved using speckle tracking [12].

The framework provides several classes for modelling the speckle-tracking setup components such as source spectra, samples and detector types. The samples are represented through their complex amplitude transmission function treated in projection approximation [15]. The wavefront information in a certain plane perpendicular to the propagation direction is stored as a 2D complex-valued array representing the amplitude and phase of the wavefront in every pixel. The detector records intensity values in the observation plane.

The propagation between the setup components is modelled using the Fresnel approximation of the diffraction integral [16]:

$$\psi(x_2, y_2, z_2) = \frac{\exp(ik(z_2 - z_1))}{i\lambda(z_2 - z_1)} \iint \psi(x_1, y_1, z_1) \exp\left(ik \frac{(x_2 - x_1)^2 - (y_2 - y_1)^2}{2(z_2 - z_1)}\right) dx_1 dy_1, \quad (1)$$

where $\psi(x_2, y_2, z_2)$ is the wave field in the destination plane, $\psi(x_1, y_1, z_1)$ the wave field in the starting plane of propagation, λ represents the wavelength of the radiation and $k = 2\pi/\lambda$ the corresponding wavevector.

Experimental and simulated setup

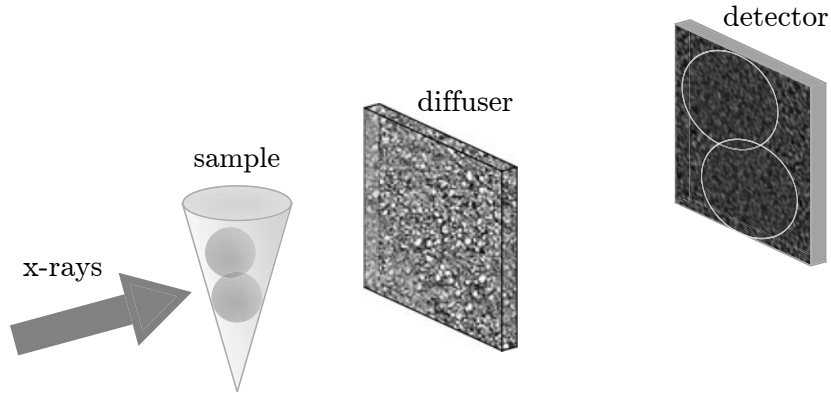


FIGURE 1. Schematic setup used for the simulations and experimental measurements. The sample consists of two PMMA spheres (1.5 mm diameter) in water. The plastic container holding the spheres was not considered in the simulations. A monochromatic x-ray beam of energy 20 keV is illuminating the sample and a random phase modulator (diffuser) producing a speckle pattern superimposed by the sample features in the detector plane. The setup parameters can be found in Tab. 1.

The setup used for this work is shown in Fig. 1. The experimental measurements were performed with a monochromatic beam of energy 20 keV from an undulator source at beamline P05 of the PETRA III synchrotron. The setup consists of a static random phase modulator (diffuser) producing a speckle pattern, a demonstrator sample formed by two polymethylmethacrylate (PMMA) spheres with 1.5 mm diameter in water, and the detector that records the intensity of the wavefront. A list of the experimental parameters, also used for the simulations, is reported in Tab. 1.

The diffuser was a piece of cellulose acetate biological filter membrane with pore size 1.2 μm . It was modelled as a three-dimensional volume consisting of stacked cellulose acetate¹ layers perforated by holes of 1.2 μm diameter. In the simulation, the diffuser was illuminated by a monochromatic parallel beam of energy 20 keV. The spheres forming the sample were placed in a plastic container for the synchrotron measurements. However, in the simulation, the container

¹ chemical formula $\text{C}_{10}\text{H}_{14}\text{O}_7$, density 1.28 g/cm³

TABLE 1. Experimental parameters used for the simulation.

X-ray energy	20 keV
Sample-diffuser distance	0.385 m
Sample-detector distance	1.420 m
Source-to-sample distance	80 m
Detector pixel size	1.14 μm

was not considered and only spheres in water were modelled. The influence of a finite source size was taken into account by applying a Gaussian smoother to the simulated recorded wavefront in the detector plane. In accordance with the experimental measurements at the synchrotron, a source with the dimensions $\sigma_x = 37.0 \mu\text{m}$ in the horizontal and $\sigma_y = 5.7 \mu\text{m}$ in the vertical direction was assumed at a distance of 80 m from the sample, leading to a projected source size in the detector plane of $\Sigma_x = 0.66 \mu\text{m}$ in the horizontal and $\Sigma_y = 0.10 \mu\text{m}$ in the vertical direction. The detector was a back-illuminated CCD camera system with an effective pixel size of $1.14 \mu\text{m}$ and an estimated point spread function of 3.5 pixels full-width-at-half maximum (FWHM). The detector response was simulated through the convolution of the final images with a symmetric Gaussian of $\sigma_{\text{det}} = 1.7 \mu\text{m}$. The exposure time for the reference image (only speckles) as well as for the sample image superimposed to the speckle pattern was 2 seconds, while no noise was taken into account in the simulations.

RESULTS

The simulated (top) and experimentally measured (bottom) near-field speckle patterns, without sample in the beam (reference pattern) and with sample in the beam, are shown in Fig. 2. The distortions of the speckle pattern induced by the sample are highlighted in the zoomed areas at the right (Fig. 2(c) and 2(f)). We note that the speckles are clearly visible for both the experimental and the simulated case, but that the speckle shape and size are slightly different. In particular, the speckles seem to be larger and horizontally elongated in the experimental data. This might be due to imprecisions in the simulations of the diffusing membrane and/or imperfections and instabilities in the optical elements of the beamline that were not taken into account in the simulations. Low-spatial frequency variations in the intensity of the experimental data are caused by beam inhomogeneities which were not reproduced in the numerical simulations. In both Figs. 2(c) and 2(f), the interface sphere-water is clearly visible as a brighter line in the zoomed-in areas. The increased intensity at the interface is due to the edge-enhancement effect.

The algorithm used to analyse the distortions of the speckle pattern caused by the sample and to convert them into image signals is described elsewhere [9]. The refraction angle, transmission and visibility-contrast (dark-field) images obtained with this algorithm are shown in Fig. 3 for both the simulated (top) and the experimental (bottom) case. Through visual comparison of the images in Fig. 3, we find that the signals retrieved from the experimental and the simulated data are in good agreement. In particular, the refraction angle values in the vertical direction (see Figs. 3(b) and 3(f)) compare well quantitatively as illustrated in Fig. 3(i) showing the vertical line profiles through the centre of the right sphere.

The major discrepancy between the signals from the experimental and the simulated data is found for the horizontal component of the refraction angle and for the transmission data because these signals are sensitive to the presence of the plastic container that was not taken into account in the simulations. The container also leads to an additional refraction, which can be observed as a slight offset in Fig. 3(i) of the refraction values for the experimental case with respect to the simulated case.

The vertical container walls are visible in Figs. 3(e) and 3(g). The noise at the edges of the spheres in the refraction angle images in both the experimental and the simulated data is caused by the substantial speckle distortions in these areas. At the edges, the correlation algorithm used to analyse the speckle distortions fails to track the speckle displacement. On the other hand, the edge-enhancement signal at the interface spheres-water is the dominant source of contrast in the transmission data. The (mainly horizontal) high-spatial frequency features in Fig. 3(g) are caused by beam instabilities: the beam slightly moved between acquisition of the reference image and the image of the sample. The phantom is completely composed of homogeneous materials (water and plastic spheres). Thus, no visibility contrast is expected in this case, also because a monochromatic beam was used. The only signal observed in the

visibility-contrast images in Figs. 3(d) and 3(h) is at the edges of the sphere and at the walls of the plastic container, where the shape of the speckles is severely affected by strong refraction.

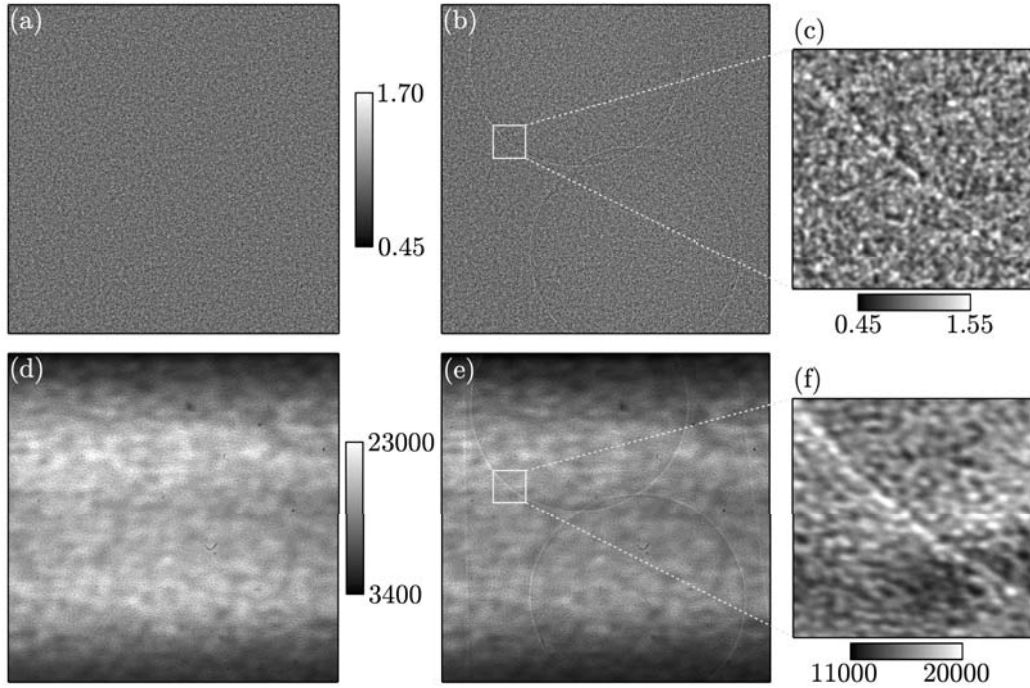


FIGURE 2. Speckle pattern created by the diffusing membrane. Panel (a) shows the simulated near-field speckle pattern with the diffuser only and panel (b) the pattern with sample and diffuser in the beam. In inset window (c) a region of interest (200×200 pixels) of panel (b) is displayed. Panels (d) and (e) show the diffuser-only and sample-and-diffuser speckle patterns for the experimental case, and panel (f) a 200×200 pixels region of interest of the pattern in panel (e). Simulated and experimental data show a fine speckle pattern. For the experimental case the speckles are elongated more severely which can be explained by beam or mechanical instabilities and other factors not taken into account in the simulations.

CONCLUSIONS

The simulation software presented in this paper allows to model image formation in speckle-based multi-contrast x-ray imaging. We demonstrated the reliability of our software through comparison of simulated images of a phantom sample with known geometry with experimental data obtained with a synchrotron source. All the image signals experimentally obtained with speckle-based x-ray imaging could be well reproduced by our simulation software. When further parameters will be included in the simulation, such as noise properties, and exact detector response, it will be a useful tool to predict the optimal parameters for a specific experiment. Moreover, similarly to speckle-based imaging, more advanced techniques based on the use of near-field speckles, such as near-field ptychography [17], can be modelled and thoroughly investigated.

ACKNOWLEDGMENTS

We acknowledge financial support from the DFG Cluster of Excellence Munich-Centre for Advanced Photonics (MAP), the DFG Gottfried Wilhelm Leibniz program and the European Research Council (ERC, FP7, StG 240142 & 279753). We acknowledge Tunhe Zhou and Anna Burvall from KTH, Stockholm for fruitful discussions.

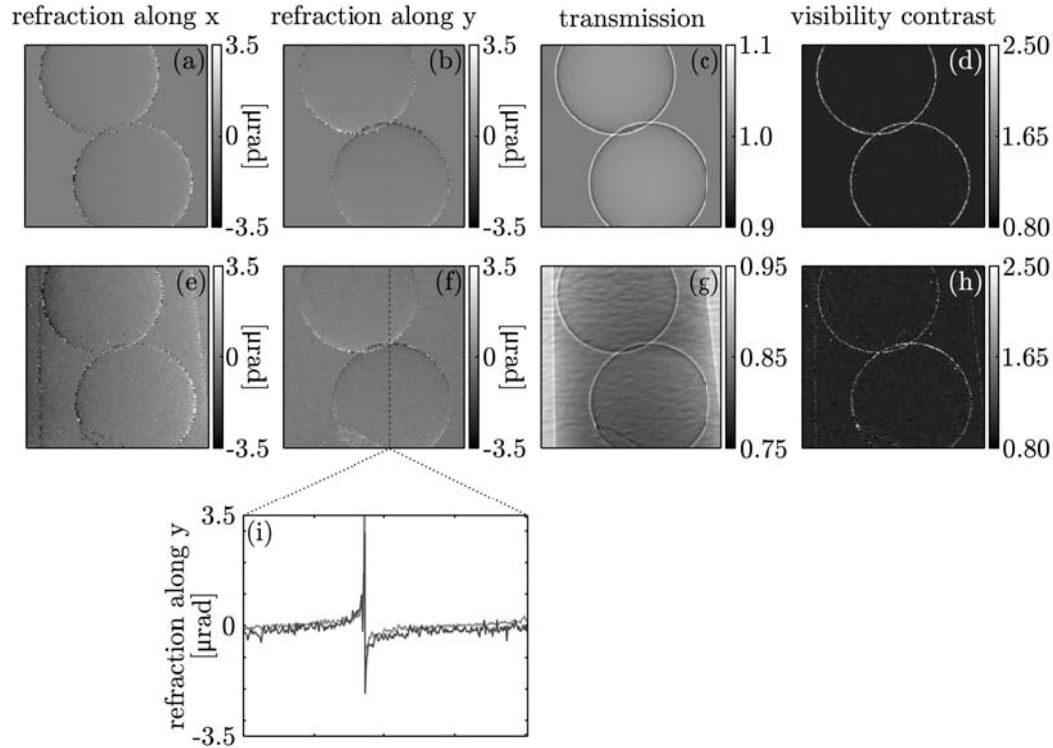


FIGURE 3. Reconstructed multimodal signals of the two PMMA spheres (1.5 mm diameter) in water retrieved from the simulation data (panels (a)–(d)) and the experimental measurement (panels (e)–(h)). Panel (i) shows the vertical profiles through the centre of the right sphere indicated by the dashed lines in panels (b) (red line) and (f) (blue line). The refraction along y for the simulated and the experimental cases are in good agreement. The mismatch between panels (a) and (e) and panels (c) and (g) is due to the plastic container holding the spheres, which was not taken into account in the simulation.

REFERENCES

1. I. Zanette, M. Bech, A. Rack, G. Le Duc, P. Tafforeau, C. David, J. Mohr, F. Pfeiffer, and T. Weitkamp, *Proc. Natl. Acad. Sci. U.S.A.* **109**, 10199–10204 (2012).
2. A. Velroyen, M. Bech, I. Zanette, J. Schwarz, A. Rack, C. Tympner, T. Herrler, C. Staab-Weijnitz, M. Braunagel, M. Reiser, F. Bamberg, F. Pfeiffer, and M. Notohamiprodjo, *PLoS ONE* **9**, e109562 (2014).
3. A. Malecki, G. Potdevin, and F. Pfeiffer, *Europhys. Lett.* **99**, 48001 (2012).
4. K. S. Morgan, D. M. Paganin, and K. K. W. Siu, *Appl. Phys. Lett.* **100**, 124102 (2012).
5. S. Berujon, H. Wang, and K. Sawhney, *Phys. Rev. A* **86**, 063813 (2012).
6. S. Berujon, E. Ziegler, R. Cerbino, and L. Peverini, *Phys. Rev. Lett.* **108**, 158102 (2012).
7. H. Wang, Y. Kashyap, and K. Sawhney, *Phys. Rev. Lett.* **114**, 103901 (2015).
8. H. Wang, S. Berujon, J. Herzen, R. Atwood, D. Laundy, A. Hipp, and K. Sawhney, *Sci. Rep.* **5** (2015).
9. I. Zanette, T. Zhou, A. Burvall, U. Lundström, D. H. Larsson, M. Zdora, P. Thibault, F. Pfeiffer, and H. M. Hertz, *Phys. Rev. Lett.* **112**, 253903 (2014).
10. T. Zhou, I. Zanette, M. Zdora, U. Lundström, D. H. Larsson, H. M. Hertz, F. Pfeiffer, and A. Burvall, *Opt. Lett.* **40**, 2822–2825 (2015).
11. R. Cerbino, L. Peverini, M. Potenza, A. Robert, P. Bosecke, and M. Giglio, *Nature Phys.* **4**, 238–243 (2008).
12. M. Zdora, P. Thibault, F. Pfeiffer, and I. Zanette (submitted).
13. A. Malecki, *X-Ray Tensor Tomography*, Ph.D. thesis, Technische Universität München (2013).
14. J. Wolf, A. Malecki, J. Sperl, M. Chabior, M. Schüttler, D. Bequé, C. Cozzini, and F. Pfeiffer, *Biomed. Opt. Express* **5**, 3739–3747 (2014).
15. M. Born, and E. Wolf, *Principles of Optics: Electromagnetic theory of propagation, interference and diffraction of light*, Cambridge University Press, Cambridge, 1998.
16. J. W. Goodman, *Introduction to Fourier Optics*, Roberts & Company Publishers, Englewood, Colorado USA, 2004, third edn.
17. M. Stockmar, P. Cloetens, I. Zanette, B. Enders, M. Dierolf, F. Pfeiffer, and P. Thibault, *Sci. Rep.* **3** (2013).